



# The effects of bed form roughness on total suspended load via the Lattice Boltzmann Method

G.C. Yang<sup>a</sup>, C.Y. Kwok<sup>a,\*</sup>, Y.D. Sobral<sup>b</sup>

<sup>a</sup> Department of Civil Engineering, The University of Hong Kong, Haking Wong Building, Pokfulam Road, Hong Kong

<sup>b</sup> Departamento de Matemática, Universidade de Brasília, Campus Universitário Darcy Ribeiro, Brasília 70910-900, DF, Brazil

## ARTICLE INFO

### Article history:

Received 25 September 2017

Revised 19 June 2018

Accepted 4 July 2018

### Keywords:

Sediment transport

Bed form

Suspended load

Lattice Boltzmann

Turbulence

Free surface

## ABSTRACT

Bed forms in natural rivers and man-made channels provide the dominant contribution to overall flow resistance and hence significantly affect sediment transport rate. Many laboratory experiments and field observations have been conducted on bed forms, and it was found that theoretical flat-bed assumptions do not give the correct estimation for the total suspended load (TSL). In this study, we present a systematic numerical investigation of turbulent open-channel flows over bed forms using the Lattice Boltzmann Method (LBM). A static Smagorinsky model is incorporated into LBM to account for turbulence, and the dynamic interface between fluid and air is captured by a free-surface model. The time-averaged flow velocity, turbulence intensity and Reynolds shear stress in LBM simulations show an excellent agreement with the available experimental data. In addition, the coherent flow structures induced by the bed forms qualitatively agree with previous numerical results from Large Eddy Simulations based the Navier–Stokes equations. We then proceed to investigate the effects of bed form roughness, quantified by the total friction factor  $f_T$ , on sediment transport. It is found that the prediction of the TSL based on the theoretical flat-bed assumptions may lead to an overestimation of up to 30%, depending on the bed form roughness. In addition, the normalized TSL is linearly proportional to  $f_T$  and nearly inversely proportional to the ratio of downward settling velocity and upward turbulence induced diffusion. Our work proposes a general law linking these quantities to estimate the TSL, which has the potential for a more efficient and accurate engineering design of man-made channels and improved river management.

© 2018 Elsevier Inc. All rights reserved.

## 1. Introduction

Bed forms are present in nearly all fluvial channels and play an important role in dictating flow resistance, sediment transport and deposition. The presence of bed forms may alter the flow field and consequently affect the sediment transport in suspension. Generally, the strong wakes resulting from flow separation behind each bed form element will lead to an increase in the overall turbulence levels, and hence an extra turbulence induced diffusion that is able to enhance the flow capacity to carry sediments in suspension [1]. The increase of suspension concentration is one of the major sources of water pollutants which may harm the aquatic ecology [2]. Therefore, an in-depth study of the relationship between bed forms and sediments in suspension is of vital importance both in economy and in ecology.

\* Corresponding author.

E-mail address: [fiona.kwok@hku.hk](mailto:fiona.kwok@hku.hk) (C.Y. Kwok).

**Notation**

$u, v$	instantaneous flow velocities in $x$ - and $y$ -direction
$\bar{u}, \bar{v}$	time-averaged flow velocities in $x$ - and $y$ -direction
$u', v'$	velocity fluctuations in $x$ - and $y$ -direction
$u_{sd}, v_{sd}$	turbulence intensities in $x$ - and $y$ -direction
$\tau_{Re}$	Reynolds shear stress ( $-\rho u'v'$ )
$\rho$	fluid density
$C$	sediment concentration
$\mathbf{u}_p$	velocity of the suspended sediments
$\boldsymbol{\varepsilon}$	diffusivity tensor of the sediments
$w$	settling velocity of the sediments
$x, y$	streamwise and wall-normal directions
$\boldsymbol{\varepsilon}^m$	momentum diffusivity tensor
$\gamma$	proportionality between $\boldsymbol{\varepsilon}$ and $\boldsymbol{\varepsilon}^m$
$f_i$	density distribution function in the $i$ th direction
$\mathbf{x}$	position of the lattice cell
$\mathbf{c}_i$	lattice speed in the $i$ -th direction
$\delta_t$	time step
$t$	simulation time
$\tau_0$	relaxation coefficient
$f_i^{eq}$	equilibrium density distribution function
$\mathbf{u}$	fluid velocity
$p$	fluid pressure
$c_s$	lattice speed of sound
Re	Reynolds number
$L_{lu}$	characteristic length in lattice units
$U_{lu}$	characteristic velocity in lattice units
$\nu_0$	fluid kinematic viscosity in lattice units
$\nu_{total}$	total fluid viscosity in lattice units
$\nu_{eddy}$	turbulence eddy viscosity in lattice units
$\tau_{total}$	effective relaxation time
$C_s$	Smagorinsky constant
$\Delta$	filtered length of the Smagorinsky model
$S$	large eddy strain rate tensor
$\alpha, \beta$	spatial indices
$\pi_{\alpha\beta}^{neq}$	sum of the second-order moments of the nonequilibrium $f_i$
$\Pi$	magnitude of the tensor $\pi_{\alpha\beta}^{neq}$
$\eta$	fluid fraction of a lattice cell
$m$	fluid mass inside a lattice cell
$\rho_A$	density of the gas phase
$\mathbf{n}$	surface normal vector
$\kappa$	small offset for cell type conversion
$L$	resolution of the cavity flow or the periodic length of the bed forms
$U$	velocity of the upper boundary in the cavity flow or mean flow velocity
$h_w$	height of the residual water column
$x_w$	advance of the collapsing water column
$H_i, L_i$	initial height and length of the water column
$L_r, L_t$	lengths of the recirculation region and the flume
$L_e$	distance between the entrance and the measured section
$h$	height of the bed form element
$H$	mean depth of the fluid flow
$\mu, \sigma$	mean value and standard deviation
$u_*$	total shear velocity
Fr	Froude number
$g$	gravitational acceleration
$S$	slope of the inclined open channel
$W$	width of the open channel

$f_T$	total friction factor
$\tau_w$	wall shear stress
$\omega_z$	vorticity in the spanwise direction
$y_0$	reference level
$C_0$	sediment concentration at the reference level
$\Delta y$	resolution equal to the lattice spacing
$Z$	weighting factor
$y_s$	level of the free surface
$q_s$	normalized total suspended load
$q_{sf}$	normalized total suspended load based on the flat-bed assumptions
$q_{ss}$	normalized total suspended load based on the simulation results
$a_1, a_2, a_3$	fitting parameters
$Q$	regularized total suspended load $q_{ss}Z^{a_3}$

Numerous laboratory tests [1,3–5] and field measurements [6,7] of flow over bed forms have been conducted. Lyn [4] carried out experiments on open channel flows of constant mean depth over periodic bed forms with two different triangular shapes. Interestingly, it was found that the flat-bed assumption may grossly overestimate the local suspended sediment concentration (SSC) and the total suspended load (TSL). A recent field study of flows over bed forms was carried out by Holmes and Garcia [6] on the Missouri River. It was shown that the large river-scale and laboratory-scale flows have the similar characteristics, with flow separation at the crest of bed form element and flow reattachment on the stoss side of the next bed form element. Nevertheless, due to the wake and turbulence induced by bed forms [1,3,4], a lack of flow similarity can be expected at the near-bed region.

The previous experimental study [4] has already shown that the TSL in rivers can be significantly altered by the formation of bed forms. It is because of the complex flow structures induced by the bed forms, which are believed to be the dominating factor to sediment transport [8]. However, it is rather difficult to capture these coherent structures in experiments due to the lack of spatial and temporal resolutions. Furthermore, there is still a lack of relationship that can quantitatively describe the effects of bed forms with various configurations on the SSC and the TSL.

To complement the limited data measured in experiments, simulations of flow over bed forms have been carried out using a variety of numerical techniques based on Computational Fluid Dynamics (CFD) [9–14]. Yoon and Patel [9] used the Reynolds-averaged Navier–Stokes (RANS) method [15–17] with the  $k-\omega$  model from Wilcox [15] to study the effect of bed forms with various wavelengths and heights on the flow resistance. Mendoza and Shen [10] simulated turbulent flow over dune-like bed forms using the RANS method with the Algebraic Stress Model for the Reynolds stress [18]. The RANS results were in good agreement with the measured experimental data in terms of the mean flow velocity profiles and the Reynolds shear stress profiles. In addition, it was observed that for bed forms with large friction factor, the form resistance dominates over the bed-skin resistance [10]. However, the RANS method does not offer an instantaneous flow field [16,17]. Consequently, the turbulence coherent structures, which are responsible for sediment transport, are still unattainable.

More recent simulations have been performed using the Large Eddy Simulation (LES) method [19] in which the large-scale eddies are fully resolved, whereas the small sub-grid scale (SGS) eddies are modeled by turbulence models [16,17,20]. Yue et al. [11] simulated turbulent open-channel flow over two-dimensional (2D) bed forms using LES with the free-surface simulated by a level set method [21]. In the flow with depth equal to 6.6 times of the dune height, large vortical structures were generated at the dune crest and the formation of streaky near wall structures were also observed after flow reattachment. The evolution and dynamics of the coherent structures and their interactions with the main body of the flow, as well as the free-surface were further detailed in the reference [12–14]. However, LES simulations based on Navier–Stokes equations are still computationally expensive. And special attentions, regarding to boundary method, mesh generation and near-wall spatial resolution, are always required to accurately describe the solid wall boundaries.

Alternatively, the Lattice Boltzmann Method (LBM) has become a reliable numerical technique to simulate fluid flows, with a detailed review provided by Chen and Doolen [22]. Compared to conventional CFD, LBM is particularly successful in multiphase fluid flows and problems involving complex boundary conditions. Besides benefiting from the localized operation of the lattice Boltzmann equation, LBM is highly parallelizable in high performance computers (HPC). In addition, no iteration is required to solve for the flow velocity field and pressure field, which makes LBM in general much more efficient than the Navier–Stokes approaches, especially for transient problems [23].

Previous numerical studies [9–14] mainly focus on the flow patterns altered by the bed forms. While the goal of this study is to quantitatively investigate the effects of bed forms on the TSL based on the diffusional theory for suspensions [24]. The effects of bed forms with various configurations are quantified by their roughness with a total friction factor,  $f_T$  [25,26]. Numerical simulations are performed to provide accurate velocity and Reynolds shear stress profiles for the analysis of SSC and TSL, instead of relying on the theoretical flat-bed assumptions [24]. We choose LBM, as the first attempt, to capture the complex behaviors of turbulent flow over bed forms in an accurate and efficient manner. LBM is extended by incorporating the Smagorinsky sub-grid scale model [27] to simulate the effects of unresolved small eddies in turbulence. Also, a free-surface boundary [28] is incorporated to capture the dynamic interface between fluid and air.

This work is organized as follows: [Section 2](#) first introduces the diffusional theory for suspensions, followed by a detailed formulation of the lattice Boltzmann algorithm. Then, the Smagorinsky SGS model and the free-surface model are verified against the driven cavity flow problem and the dam-break problem in [Section 3](#). [Section 4](#) presents the simulations of turbulent flow over bed forms. The model is validated against the experimental data available in the literature and is compared to previous LES simulations based on the Navier–Stokes equations. In [Section 5](#), the effects of bed form roughness on the flow transport properties are evaluated.

## 2. Theoretical background

### 2.1. Turbulence

Turbulence fluctuations are one of the major causes to the suspension of sediments. In this study, although simulations of turbulent flow over bed forms are conducted in three dimensions, which are necessary to capture correctly the basic turbulence dynamics, analysis is carried out mainly in the streamwise ( $x$ ) and wall-normal ( $y$ ) directions. Make  $u$  and  $v$  be the instantaneous velocity components,  $\bar{u}$  and  $\bar{v}$  be the mean velocity components in  $x$  and  $y$  directions, respectively. The corresponding components of turbulence fluctuations,  $u'$  and  $v'$ , can be defined as [\[29\]](#):

$$u = \bar{u} + u', \quad v = \bar{v} + v'. \quad (1)$$

The standard deviation of the instantaneous velocity,  $u_{sd}$  or  $v_{sd}$ , is taken as a measure of turbulence intensity. Reynolds shear stress ( $\tau_{Re}$ ) is given by the average of the velocity fluctuations as [\[29\]](#):

$$\tau_{Re} = -\rho \overline{u'v'} \quad (2)$$

where  $\rho$  is the fluid density.

### 2.2. Diffusional theory for suspensions

The dynamics of the suspended particles of the flow can be described by an advection-diffusion equation written as:

$$\frac{\partial C}{\partial t} + \mathbf{u}_p \cdot \nabla C = \nabla \cdot (\boldsymbol{\varepsilon} \cdot \nabla C), \quad (3)$$

where  $C$  stands for the concentration of particles,  $t$  for the time,  $\mathbf{u}_p$  for the velocity of the dispersed particles and  $\boldsymbol{\varepsilon}$  is the diffusivity tensor of the particles.

In this work, it is assumed that the particles are passively transported by the fluid with the local mean velocity of the flow. Since the particles considered here are not neutrally buoyant, they have a settling velocity  $-w\mathbf{e}_y$ , that depends on the properties of the particles (e.g. density and diameter). Therefore, the velocity of the particles is given by:

$$\mathbf{u}_p = (\bar{u}, \bar{v} - w). \quad (4)$$

Note here that we are only considering the two-dimensional (2D) central cross-section of the channel. In this case, the diffusivity tensor is given by:

$$\boldsymbol{\varepsilon} = \begin{bmatrix} \varepsilon_{xx} & \varepsilon_{xy} \\ \varepsilon_{yx} & \varepsilon_{yy} \end{bmatrix}, \quad (5)$$

and [Eq. \(3\)](#) becomes:

$$\frac{\partial C}{\partial t} + \bar{u} \frac{\partial C}{\partial x} + (\bar{v} - w) \frac{\partial C}{\partial y} = \frac{\partial}{\partial x} \left[ \varepsilon_{xx} \frac{\partial C}{\partial x} + \varepsilon_{xy} \frac{\partial C}{\partial y} \right] + \frac{\partial}{\partial y} \left[ \varepsilon_{yx} \frac{\partial C}{\partial x} + \varepsilon_{yy} \frac{\partial C}{\partial y} \right]. \quad (6)$$

Assuming that the flow is steady and homogeneous along the  $x$ -direction, and that it has zero mean vertical velocity, [Eq. \(6\)](#) can be written as:

$$-w \frac{\partial C}{\partial y} = \frac{\partial}{\partial y} \left( \varepsilon_{yy} \frac{\partial C}{\partial y} \right). \quad (7)$$

[Eq. \(7\)](#) can be integrated with respect to  $y$ , which yields:

$$-wC - \varepsilon_{yy} \frac{\partial C}{\partial y} = f(x), \quad (8)$$

where  $f(x)$  is an arbitrary function of  $x$ . Since the flow is homogeneous in  $x$ , and the left-hand side (LHS) of [Eq. \(8\)](#) represents the net flux of particles across a horizontal plane, therefore,  $f(x) = \text{constant} = 0$ , and [Eq. \(8\)](#) becomes:

$$-wC - \varepsilon_{yy} \frac{\partial C}{\partial y} = 0. \quad (9)$$

This equation was originally obtained by Schimdt [\[30\]](#) in a different context of particle transport.

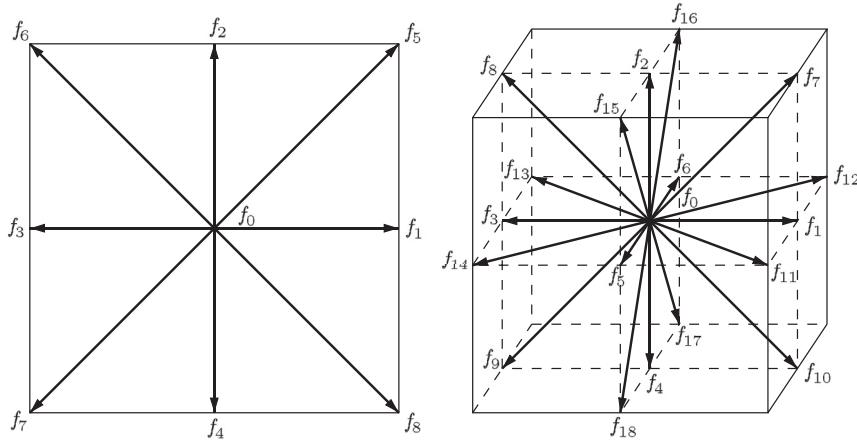


Fig. 1. Lattice structures: (a) D2Q9 for 2D problems; (b) D3Q19 for 3D problems.

In order to solve Eq. (9), the particle diffusivity  $\varepsilon_{yy} = \varepsilon_{yy}(y)$  has to be determined. The particle diffusivity should take into account the diffusion of particles that is induced by the turbulent motion of the fluid. It is assumed that the turbulence-induced diffusion due to velocity fluctuations is of much larger intensity than any other diffusional mechanism that could induce particle dispersion. Based on this assumption, and on the assumption that the particles are passively carried by the flow, it is proposed that the particle diffusivity is proportional to the momentum diffusivity, that is,

$$\boldsymbol{\varepsilon} = \gamma \boldsymbol{\varepsilon}^m, \tag{10}$$

where  $\boldsymbol{\varepsilon}^m$  is the momentum diffusivity tensor. The coefficient of proportionality between  $\boldsymbol{\varepsilon}$  and  $\boldsymbol{\varepsilon}^m$  is denoted as  $\gamma$ .

The turbulence-induced diffusion of particles is due to the velocity fluctuations of the flow that generate an extra shear stress ( $\tau_{Re}$ ) that suspends and diffuses particles. From the mixing length theory [31], the Reynolds shear stress is linked to the local mean gradient velocity of the flow, that is,

$$\tau_{Re} = \rho \varepsilon_{yy}^m \frac{\partial \bar{u}}{\partial y}. \tag{11}$$

Since both  $\tau_{Re}$  (see Eq. (2)) and the velocity gradient are known from the flow, we can deduce that the particle diffusivity is given by:

$$\varepsilon_{yy} = -\gamma \rho \frac{\overline{u'v'}}{\frac{\partial \bar{u}}{\partial y}}. \tag{12}$$

### 2.3. Lattice Boltzmann formulation

LBM is a mesoscopic description of fluid flow based on the kinetic theory [22] and is able to describe the fluid system by a collection of molecules residing on a regular lattice. A set of density distribution functions are used to represent the collection of molecules at each lattice node, where collisions between a group of molecules take place by following the conservation laws of mass, momentum and energy. At each time step, the post-collision density distribution functions are passed to the neighboring lattice nodes by a streaming process, described in [22].

In LBM, the evolution equation for the density distribution function  $f_i(\mathbf{x}, t)$  with a BGK approximation (named after Bhatnagar, Gross, and Krook) [32], can be written as:

$$f_i(\mathbf{x} + \mathbf{c}_i \delta_t, t + \delta_t) - f_i(\mathbf{x}, t) = -\frac{1}{\tau_0} [f_i(\mathbf{x}, t) - f_i^{eq}(\mathbf{x}, t)], \tag{13}$$

where the density distribution function  $f_i$  is related to the number of molecules at time  $t$  positioned at  $\mathbf{x}$  moving with velocity  $\mathbf{c}_i$  along the  $i$ -th direction at each lattice node. Fig. 1 shows the lattice structures D2Q9 and D3Q19 used for two-dimensional and three-dimensional (3D) problems. The time step for evolution and the relaxation time are  $\delta_t$  and  $\tau_0$ , respectively. The equilibrium distribution function (EDF) is  $f_i^{eq}$ . Based on the conservation of mass and momentum, the fluid density  $\rho$  and velocity  $\mathbf{u}$  can be easily reconstructed from the velocity moments of the discrete density distribution functions [22]:

$$\rho = \sum_i f_i, \tag{14}$$

$$\rho \mathbf{u} = \sum_i \mathbf{c}_i f_i. \tag{15}$$

The pressure field  $p$  is related to the fluid density by the equation of state:

$$p = c_s^2 \rho, \quad (16)$$

where  $c_s$  is the lattice speed of sound and equal to  $1/\sqrt{3}$  for both D2Q9 and D3Q19 lattice structures [22].

#### 2.4. Smagorinsky subgrid scale model

Normally, a fluid flow becomes turbulent when the Reynolds number (Re) is large. It is defined by:

$$\text{Re} = \frac{L_{lu} U_{lu}}{\nu_0}, \quad (17)$$

where  $L_{lu}$  and  $U_{lu}$  are the characteristic length and velocity in lattice units, respectively, and  $\nu_0$  is the kinematic viscosity in lattice units that is related to the relaxation time  $\tau_0$  by:

$$\nu_0 = c_s^2 \left( \tau_0 - \frac{1}{2} \right). \quad (18)$$

According to Eq. (17), a high Reynolds number can be achieved by a large value of  $L_{lu}$ . However, a large  $L_{lu}$  requires large number of lattice cells across the characteristic length which means high resolution. Therefore, there is a constraint to the maximum value of Reynolds number due to the computational limit. In addition, it is also not an option to increase the characteristic velocity  $U_{lu}$  to achieve a high Reynolds number as  $U_{lu}$  needs to be small to ensure the small value of Mach number for incompressible fluid. The only way to achieve high Reynolds number is to have a small  $\nu_0$ , and hence a  $\tau_0$  close to 0.5, according to Eq. (18).

In this study, the standard Smagorinsky SGS model proposed by Hou et al. [27] is incorporated into LBM, taking the effects from unresolved small scale eddies into consideration. The detailed Smagorinsky SGS model is available in the reference [27], and the key equations are summarized in the following.

The total fluid viscosity ( $\nu_{total}$ ) equals to the sum of the molecular viscosity ( $\nu_0$ ) and the turbulence eddy viscosity ( $\nu_{eddy}$ ):

$$\nu_{total} = \nu_0 + \nu_{eddy} = c_s^2 \left( \tau_{total} - \frac{1}{2} \right), \quad (19)$$

where  $\tau_{total}$  is the effective relaxation time, so that Eq. (13) becomes:

$$f_i(\mathbf{x} + \mathbf{c}_i \delta_t, t + \delta_t) - f_i(\mathbf{x}, t) = -\frac{1}{\tau_{total}} [f_i(\mathbf{x}, t) - f_i^{eq}(\mathbf{x}, t)]. \quad (20)$$

Comparing Eqs. (13) and (20), the unresolved small eddies are approximated by the eddy viscosity that is incorporated into the term  $\tau_{total}$ . In order to solve for the effective relaxation time  $\tau_{total}$ , the turbulence eddy viscosity,  $\nu_{eddy}$ , needs to be determined. For the standard Smagorinsky SGS model,  $\nu_{eddy}$  is given by:

$$\nu_{eddy} = C_s^2 \Delta^2 |S|, \quad (21)$$

where  $C_s$  is the model parameter, also known as the Smagorinsky constant,  $\Delta$  is the filtered length and is set to be equal to the lattice spacing  $\delta_x$  in LBM and  $|S| = (2S_{\alpha\beta} S_{\alpha\beta})^{1/2}$  is the magnitude of large eddy strain rate tensor, given by:

$$S_{\alpha\beta} = \frac{1}{2} \left( \frac{\partial \bar{u}_\alpha}{\partial x_\beta} + \frac{\partial \bar{u}_\beta}{\partial x_\alpha} \right), \quad (22)$$

where  $\alpha$  and  $\beta$  are the spatial indices. From the Chapman–Enskog expansion of the lattice Boltzmann equation [27], it can be found that the strain rate tensor can be calculated locally from the summation of the second-order moments of the nonequilibrium distributions in all lattice directions:

$$\pi_{\alpha\beta}^{neq} = \sum_i c_{i\alpha} c_{i\beta} (f_i - f_i^{eq}) = -2c_s^2 \rho \tau_{total} S_{\alpha\beta}, \quad (23)$$

and so:

$$\Pi = \sqrt{\pi_{\alpha\beta}^{neq} \pi_{\alpha\beta}^{neq}} = 2c_s^2 \rho \tau_{total} |S|. \quad (24)$$

If we eliminate  $|S|$  from Eqs. (21) and (24), and substitute  $\nu_{eddy}$  into Eq. (19), the effective relaxation time can be determined by:

$$\tau_{total} = \frac{\tau_0 + \sqrt{\tau_0^2 + 2C_s^2 \Delta^2 \Pi (\rho c_s^4)^{-1}}}{2} \quad (25)$$

Substituting Eq. (25) into Eq. (20), the density distribution functions at each time step can be solved. The value of the Smagorinsky constant  $C_s$  can be quite different for various problems, depending on the Reynolds number, geometry, resolution and others. For the simulation of turbulent flow over bed forms, the  $C_s$  value is adopted as 0.11 based on the parametric study presented in Section 4.2.

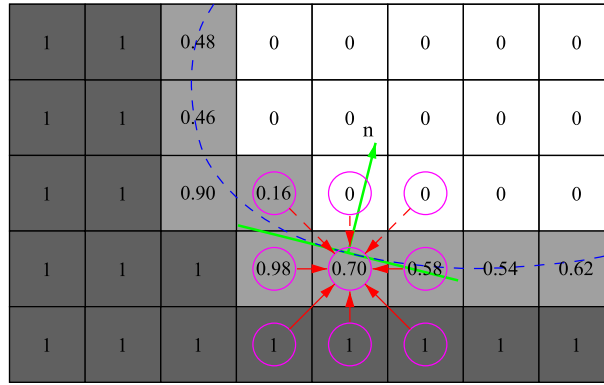


**Fig. 2.** Two-dimensional representation of lattice cells, including gas (white), interface (light gray) and fluid (dark gray). The interface cells intersected with the real surface (blue dashed curve) are characterized by the fluid volume fraction (see Eq. (26)). Reconstructions of density distribution functions are required for particles streaming from gas cells to interface cells (red dashed arrows). The surface normal,  $\mathbf{n}$ , can be estimated using Eq. (32). (For interpretation of the references to color in this figure legend, the reader is referred to the web version of this article.)

2.5. Free-surface model

A free-surface algorithm, which was initially proposed to describe the dynamic form of molten metal [28,33], is applied in this study to simulate the top surface of the open channel flow [4]. The simulation domain consists of three different types of cells: “fluid”, in which the cell is completely filled with fluid; “gas”, where the cell contains no fluid and “interface” that always exists between the fluid and gas cells and are partially filled with fluid (see Fig. 2).

The evolution of the free surface involves following three steps: a) computation of interface movement; b) reconstruction of unknown distribution functions based on the boundary conditions at the fluid interface; c) re-initialization of cell types.

2.5.1. Mass flux between interface cell and neighboring cells (fluid or interface)

In order to track the fluid-gas interface, two additional parameters are required for each cell, including mass  $m$  and fluid fraction  $\eta$ . The fluid fraction is equal to the mass of fluid present in each cell divided by the total fluid mass that the cell can accept. Considering a unit volume for each lattice cell, then:

$$\eta = \frac{m}{\rho}. \tag{26}$$

The distribution functions in LBM correspond to the number of particles, and therefore, the mass flux can be directly calculated from the difference between the distribution functions streaming into and out of the considered cell. For an interface cell at  $\mathbf{x}$  and a fluid cell at  $\mathbf{x} + \mathbf{c}_i \delta_t$ , the change of mass can be written as:

$$\Delta m_i(\mathbf{x}, t + \delta_t) = f_{i,opp}(\mathbf{x} + \mathbf{c}_i \delta_t, t) - f_i(\mathbf{x}, t). \tag{27}$$

Here, the subscript  $i$  denotes the direction leaving the cell and  $i, opp$  represents the opposite direction entering the cell. If the neighboring cell is also an interface cell, the distribution functions are multiplied by the contact area that is approximated by the average fluid fractions, that is:

$$\Delta m_i(\mathbf{x}, t + \delta_t) = [f_{i,opp}(\mathbf{x} + \mathbf{c}_i \delta_t) - f_i(\mathbf{x}, t)] \frac{\eta(\mathbf{x} + \mathbf{c}_i \delta_t, t) + \eta(\mathbf{x}, t)}{2}. \tag{28}$$

Both Eqs. (27) and (28) are completely symmetric, meaning that the amounts of fluid particles leaving one lattice cell have to enter another cell, and vice versa. In another word, the mass is intrinsically conserved:

$$\Delta m_i(\mathbf{x}, t) = -\Delta m_{i,opp}(\mathbf{x} + \mathbf{c}_i \delta_t, t). \tag{29}$$

The mass fluxes in all directions are added to the mass at the current time step for the considered interface cell to calculate the mass for the next time step:

$$m_i(\mathbf{x}, t + \delta_t) = m_i(\mathbf{x}, t) + \sum_{i=1}^n \Delta m_i(\mathbf{x}, t + \delta_t), \tag{30}$$

where  $n$  is equal to 9 for 2D problems and 19 for 3D problems.

2.5.2. Reconstruction of distribution functions streaming from gas cells

Similar to the lattice cells for solid boundaries, the distribution functions for gas cells are not accessed by assuming that the effect of gas phase on the motion of fluid phase is negligible [28]. This is a reasonable assumption for this study as long as the bulk fluid motion is concerned [11]. It is assumed that the gas phase has a density equal to  $\rho_A$  that is much

smaller than the fluid phase. It can also be considered that the gas reaches an equilibrium state much faster than the fluid. Besides, the gas and fluid shall share the same velocity ( $\mathbf{u}$ ) at the interface. Therefore, the unknown distribution functions streaming from the gas cells to the interface cells can be determined from the following equation:

$$f_{i,opp}(\mathbf{x}, t + \delta_t) = f_i^{eq}(\rho_A, \mathbf{u}) + f_{i,opp}^{eq}(\rho_A, \mathbf{u}) - f_i(\mathbf{x}, t). \quad (31)$$

In order to balance the force on each side of the free surface, so that the dynamic boundary condition is fulfilled, the distribution functions streaming from the neighboring interface cells also need to be reconstructed, using Eq. (31), if  $\mathbf{n} \cdot \mathbf{c}_i < 0$ , where  $\mathbf{n}$  is the surface normal pointing to the gas phase that can be approximated by the central difference of fluid fractions:

$$\mathbf{n} = \frac{1}{2} \begin{bmatrix} \eta(x_{j-1,k,l}) - \eta(x_{j+1,k,l}) \\ \eta(x_{j,k-1,l}) - \eta(x_{j,k+1,l}) \\ \eta(x_{j,k,l-1}) - \eta(x_{j,k,l+1}) \end{bmatrix}. \quad (32)$$

### 2.5.3. Re-initialization of cell types

All distribution functions are determined for the interface cells after the streaming and reconstruction steps. The collision steps are conducted and Eq. (14) is used to update the density for the interface cells. The conversion of interface cell into fluid or gas cell is performed by the following criteria:

$$\begin{aligned} \text{Interface cell} &\rightarrow \text{Fluid cell } m(\mathbf{x}, t + \delta_t) > (1 + \kappa)\rho(\mathbf{x}, t + \delta_t), \\ \text{Interface cell} &\rightarrow \text{Gas cell } m(\mathbf{x}, t + \delta_t) < (0 - \kappa)\rho(\mathbf{x}, t + \delta_t), \end{aligned} \quad (33)$$

where  $\kappa$  is a small offset and is set to be 0.001 to prevent new surrounding interface cells from being re-converted for the next time step [33]. For a new fluid cell, all neighboring gas cells are converted into interface cells. While for a new gas cell, all neighboring fluid cells are converted into the interface cells. The masses of fluid and gas cells are always equal to 1 and 0, respectively, resulting in excess (nonzero) mass during cell conversion. In order to maintain the mass conservation, the excess mass is distributed to the neighboring interface cells.

## 3. Verification of the code

### 3.1. Driven cavity flow at high Reynolds number

The classical two-dimensional driven cavity flow is widely used as a benchmark problem to test the efficiency and accuracy of numerical models. A comprehensive study has been conducted by Erturk [34] to characterize the flow pattern using CFD. Although a vast literature shows that the solution for driven cavity flow problem becomes unsteady once the Reynolds number is higher than 8000 [35–37] based on the velocity of the top boundary,  $U$ , it is found that the numerical instability can be avoided by increasing the resolution [38] or incorporating a turbulent model in this study. Fig. 3(a) shows the geometry of the driven cavity flow problem with 256 lattice cells in horizontal and vertical directions. In this study, LBM is applied to simulate the 2D driven cavity flow at Reynolds numbers of 1000 and 21,000.

For  $Re = 1000$ , a laminar flow is observed and the LBM simulation converges to a steady state. The horizontal and vertical velocity profiles agree well with the data available in [38] (see the square symbols and the solid lines in Fig. 3(b) and (c)). For  $Re = 21,000$ , however, it is not possible to achieve a steady state with the chosen resolution. Incorporating the Smagorinsky SGS model introduced in Section 2.4 with  $C_s = 0.3$ , a steady solution can be achieved (see the triangle symbols and the dashed lines in Fig. 3(b) and (c)). A good agreement between the LBM results and the data available in [38] proves that the Smagorinsky SGS model incorporated in the current LBM code performs effectively.

### 3.2. Three-dimensional dam break problem

The free-surface model is validated through the 3D dam break problem. Nishi and Doan [39] have conducted similar simulations in two dimension with a hybrid (partial-slip) boundary condition to take the unknown wall effects into consideration so as to reproduce the phenomenon observed in the physical experiment conducted by Martin and Moyce [40]. In the experiment, a water column with a square base of width ( $L_i$ ) equal to 5.715 cm was constrained by a thin waxed paper diaphragm and the left wall. The height of water column ( $H_i$ ) was double of the base width. As the diaphragm wall was removed, the water column started to fall down and flow rightward along the horizontal floor (see Fig. 4(a)). The evolutions of the distance between the surge front and the left wall ( $x_w$ ) and the height of residual water column ( $h_w$ ) were recorded.

The simplification of a three-dimensional dam break problem to two dimension may lead to some errors. For instance, the shape of surge front cannot be captured in two dimension, which turns out to have a significant effect on the runout distance  $x_w$ . Different from Nishi and Doan [39], no-slip boundary conditions are applied at the solid walls in the current 3D LBM model. A uniform resolution with 100 lattice cells along the initial height of the water column is applied. The numerical results in terms of the evolution of the runout distance and the height of water column are compared to the experimental data in Fig. 4(b) and (c). A reasonably good agreement is achieved. The slight discrepancy between the LBM results and the experimental data may be due to the effect of diaphragm wall removal in the physical test [40].

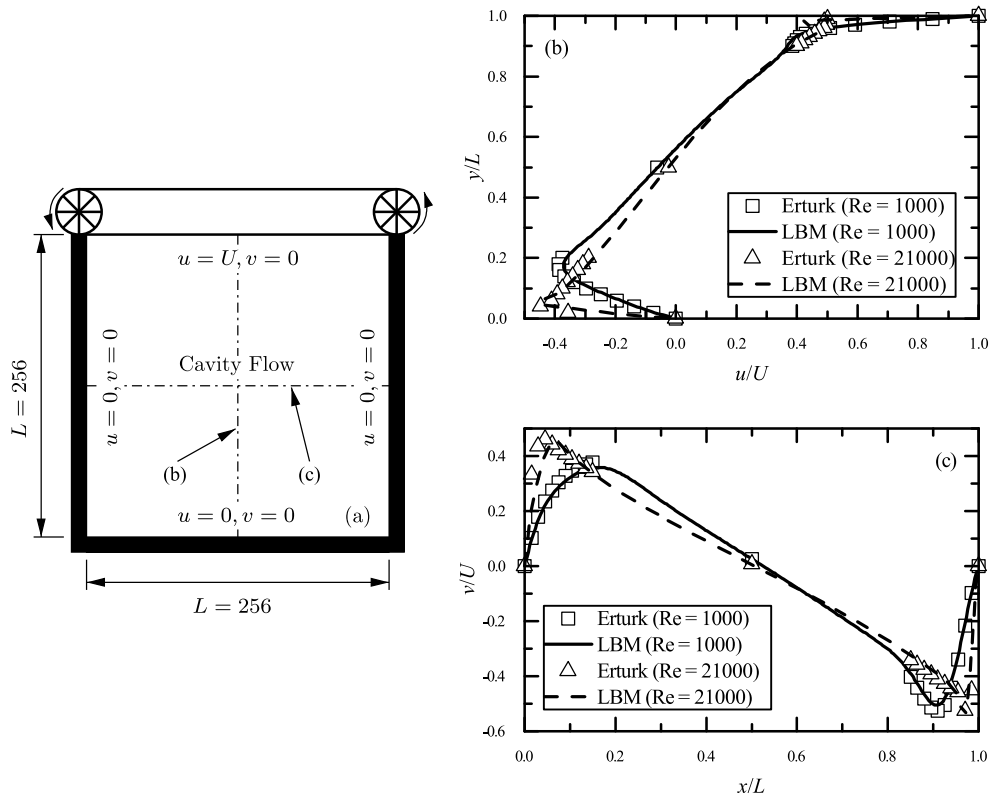


**Fig. 3.** Simulation of two-dimensional driven cavity flow problem: (a) sketch of the square cavity with 256 lattice cells in horizontal and vertical dimensions; (b) comparison between LBM results and the data available in [38] regarding to the horizontal velocity profiles along a vertical line; (c) and the vertical velocity profiles along a horizontal line passing through the geometric center of the cavity at a Reynolds number equal to 1000 and 21,000.

## 4. Simulation of turbulent flow over bed forms

### 4.1. Experimental setup and numerical model

In this section, the verified LBM code is applied to simulate the turbulent flow over bed forms. Fig. 5 shows the geometry of bed forms and the boundary conditions following the experimental setup from Lyn [4]. The bed forms are composed of triangular elements with a gentle upstream face and a steep downstream face with a 45-degree base angle (called as a dune-shape in this study). The bed forms are periodic with a peak height  $h = 1.2$  cm and a wavelength  $L = 15$  cm. The recirculating channel is approximately 13 m long (in  $x$ -direction) and 26.67 cm wide (in  $z$ -direction) with an adjustable slope. In the experiment of Lyn [4], the fluid flow was measured by Laser-Doppler Velocimetry (LDV) at positions around 9 m from the flume entrance to minimize the effect on turbulent flow from the entrance and exit. Measurements were taken at four individual positions at  $x/L = 0, 0.25, 0.5$  and  $0.75$  (see Fig. 5). The flow depth measured from the mean bed level is  $H = 6.1$  cm. All measurements are made in a longitudinal plane half-way through the spanwise length, far away from the no-slip side walls.

In the numerical model, only one period of the bed forms is simulated with periodic boundaries defined at the faces in the streamwise direction. Bounce-back dynamics, i.e. no-slip boundary conditions, are assigned to the lattice nodes located within the bed forms and also on the side walls. The free-surface model introduced in Section 2.5 is used to define the top surface of the open-channel flow. A uniform lattice spacing  $\Delta x = 1$  mm is defined throughout the whole simulation domain. A 13 mm clearance (gas phase) is initially defined to allow for the formation of a free surface. Therefore, there are  $N_{total} = 3,204,000$  lattice cells in total, as a result of  $N_x = 150$ ,  $N_y = 80$ , and  $N_z = 267$  cells in  $x$ -,  $y$ - and  $z$ -directions, respectively. The sufficiency of the lattice resolution will be addressed in Section 4.3.

In order to drive the flow, the simulated flume is tilted with the same slope equal to 0.00145 as that in the experiment. Fig. 6 shows that the mean flow velocity increases initially and becomes steady at around 28 cm/s after about 60 s. A total of 360 s of simulation is conducted. The data acquisition frequency is set to be 100 Hz, which is sufficient for stable statistics of the turbulent flow. The data obtained between 120 s and 360 s are used for the calculation of turbulent statistics at the steady state, including profiles for the time-averaged flow velocity, the turbulence intensity and the Reynolds shear stress.

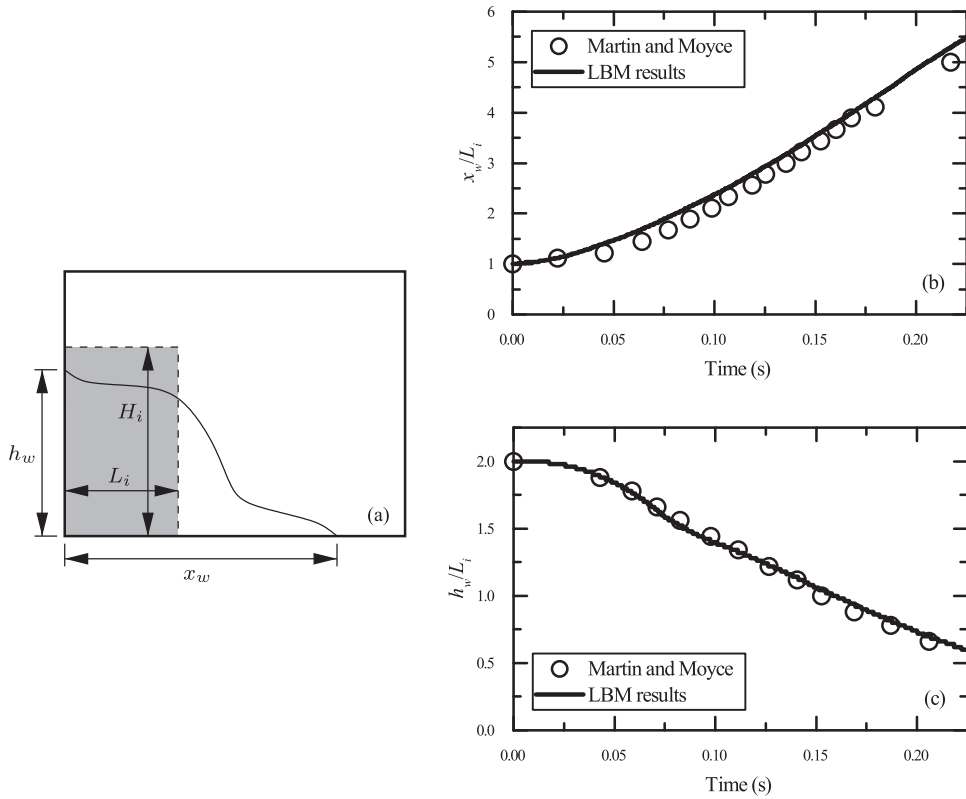


**Fig. 4.** Simulation of a three-dimensional dam break problem: (a) sketch of the geometry; (b) advance of the surge front; (c) and falling down of the water column (the step-wise curve is attributed to the spatial discretization in the numerical simulation).

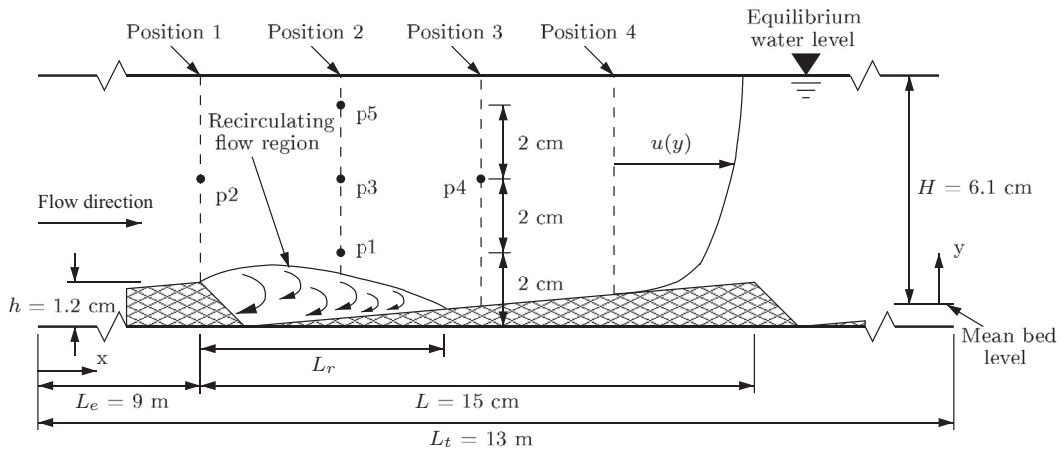


**Fig. 5.** Sketch of the experimental and numerical setup, flow conditions and bed forms.

4.2. Effect of the Smagorinsky constant

For the standard turbulent model, the Smagorinsky constant  $C_s$  needs to be calibrated. Fig. 7 shows the plot of average flow velocities at five selected points (p1–p5, see Fig. 5) for different values of the Smagorinsky constant: 0.105, 0.11, 0.12, 0.15 and 0.20. The error bars correspond to the standard deviations of the instantaneous flow velocity.

For the range of  $C_s$  from 0.105 to 0.15, the time-averaged local flow velocity decreases when  $C_s$  increases. It is because the eddy viscosity becomes larger (see Eq. (21)) and hence the total fluid viscosity increases (see Eq. (19)), resulting into a more viscous fluid and small local velocities. When  $C_s$  increases from 0.15 to 0.2, its effect on the average local flow velocity is less significant. Besides, by comparing the average flow velocities at p1 (close to the bed) and p5 (close to the free

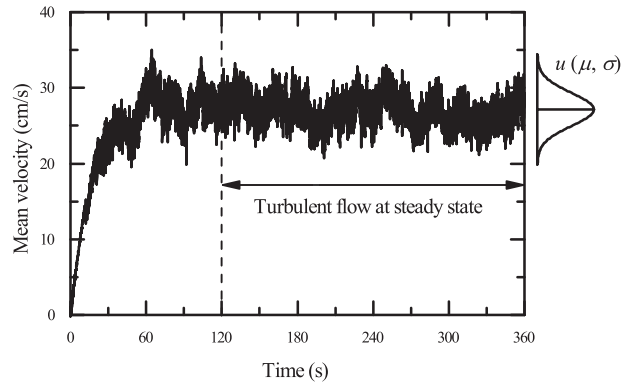


Fig. 6. Development of the mean velocity of the simulated turbulent flow at Position 4. The Smagorinsky constant is defined as  $C_s = 0.11$ .

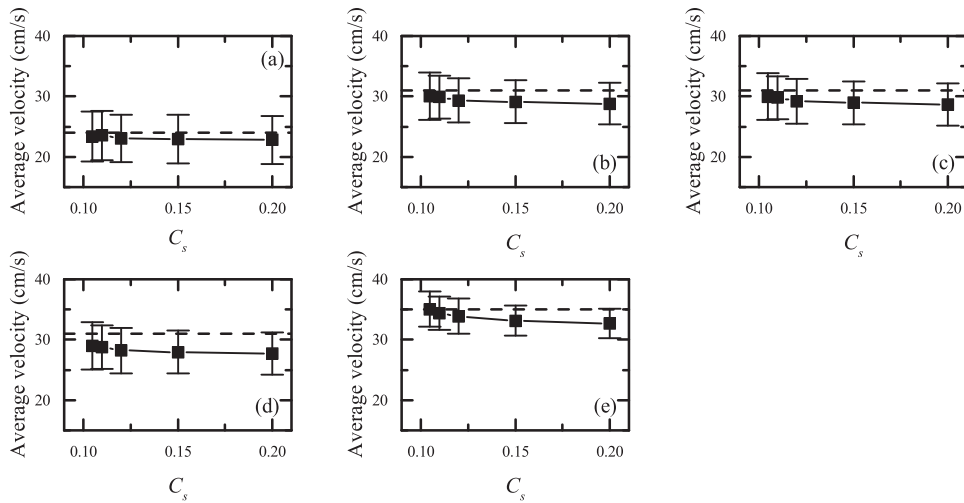


Fig. 7. Effect of the Smagorinsky constant on the time-averaged local flow velocities at (a) p1; (b) p2; (c) p3; (d) p4; and (e) p5. The dashed lines indicate the measured values from Lyn [4].

Table 1

Summary of the lattice resolution and the computational time,  $T$ , for the simulation of turbulent flow over bed forms.

Resolution	$N_x \times N_y \times N_z$	$N_{total}$	$\Delta x$ (mm)	$\Delta x/h$	$T$ (h)
RL	$90 \times 48 \times 159$	686,880	1.6750	0.1396	9.5
RN	$150 \times 80 \times 267$	3,204,000	1.0000	0.0833	57.1
RH	$179 \times 96 \times 319$	5,481,696	0.8375	0.0698	195.6

surface), it can be found that the influence of  $C_s$  is relatively larger for the flow close to the free-surface. Simulations with  $C_s$  value equal to 0.105 and 0.11 are able to match the experimental data [4] as indicated by the dashed lines in Fig. 7 in terms of the average local flow velocity quite well. The simulation with  $C_s = 0.11$  achieves a better agreement at locations close to the bed (see Fig. 7(a)), where the accuracy is of more concern for the calculation of the TSL in Section 5. Therefore,  $C_s$  is chosen to be 0.11 for the simulation of turbulent flow over bed forms in this study.

#### 4.3. Velocity, turbulence intensity and Reynolds shear stress

The time-averaged horizontal ( $\bar{u}$ ) and vertical ( $\bar{v}$ ) velocities for Position 1–4 obtained from the simulations are shown in Fig. 8, together with the experimental data. In order to demonstrate the sufficiency of the adopted spatial resolution (RN), simulations with a lower (RL) and a higher (RH) lattice resolution are performed. The adopted resolutions and the corresponding simulation times are summarized in Table 1. All cases are simulated with 6 compute nodes, each of which is equipped with two 10-core Intel Xeon E5-2600 v3 processors and 96 GB physical memory. It can be clearly seen that the simulation with RL systematically underestimates the horizontal velocity throughout the whole flow field, whereas the

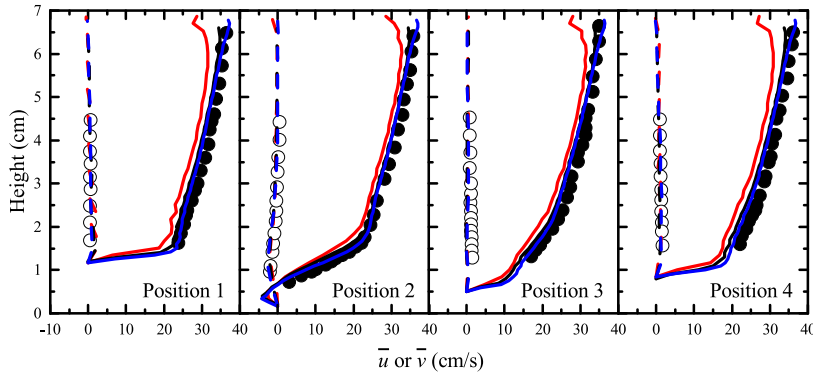


**Fig. 8.** Comparison between experimental data and LBM results in terms of the horizontal and vertical velocity profiles at Position 1–4: ●  $\bar{u}$  (experiment); ○  $\bar{v}$  (experiment); —  $\bar{u}$  (LBM RL); - -  $\bar{v}$  (LBM RL); - - -  $\bar{u}$  (LBM RN); - - -  $\bar{v}$  (LBM RN); —  $\bar{u}$  (LBM RH); - -  $\bar{v}$  (LBM RH).

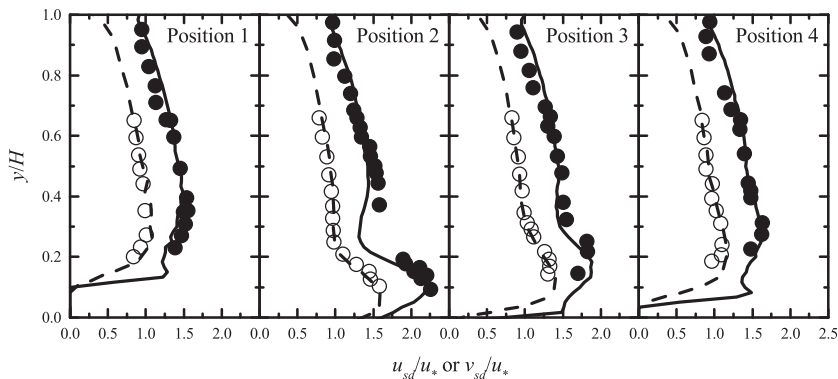


**Fig. 9.** Comparison between experimental data and LBM results in terms of the turbulence intensity profiles at Position 1–4: ●  $u_{sd}/u_*$  (experiment); ○  $v_{sd}/u_*$  (experiment); —  $u_{sd}/u_*$  (LBM); - -  $v_{sd}/u_*$  (LBM).

simulation with RH yields similar results comparable with those from the simulation using RN. However, the computational cost is significantly increased when the resolution is increased from RN to RH.

Although a reasonably good agreement between the numerical results and the experimental data is achieved with the resolution RN, two points deserve further comments. The first one is that the experimental setup used by Lyn [4] is not able to measure correctly the velocities close to the free surface. The observed reduction of horizontal velocity on that region from the numerical simulation might come from secondary circulations [11]. The second is the slightly lower horizontal velocities close to the bed in numerical simulations, where the turbulent model may not perform very well to capture the effects from small eddies close to the discretized solid boundary.

The profiles for turbulence intensities in horizontal and vertical directions are calculated and compared to the measured values in Fig. 9. Following Lyn [4], the turbulence intensities are normalized by the total shear velocity  $u_* = \sqrt{gHS}$ , where  $g$  is the gravitational acceleration and  $S$  is the mean energy slope. Again, the numerical results agree with the experimental data quite well. Note that close to the free surface, there is a slight increase in the horizontal component, which is also observed in the experiments indicating that the free surface model in LBM can realistically capture the large turbulence intensities caused by the perturbations of the free surface.

Fig. 10 compares the numerical results and experimental data regarding to the Reynolds shear stress normalized by the shear velocity  $u_*$  and, again, a good agreement is achieved. The straight dashed line represents the linear variation of shear stress corresponding to a theoretical flat-bed flow. Due to the presence of bed forms in the experiments and numerical simulations, the Reynolds shear stress profiles are significantly altered at the inner flow region ( $y/H < 0.4$ ). Peak values are observed at a level close to the crest of the bed forms. Nevertheless, at the outer flow region ( $y/H > 0.4$ ), both numerical results and experimental data collapse with the flat-bed profile quite well, indicating that the bed forms mainly influence the inner flow region.

#### 4.4. Turbulent flow structures

As this is the first attempt to simulate turbulent flow over bed forms using LBM, our numerical results are carefully compared to previously published CFD/LES results in terms of the turbulent flow structures. The spatial distribution of the

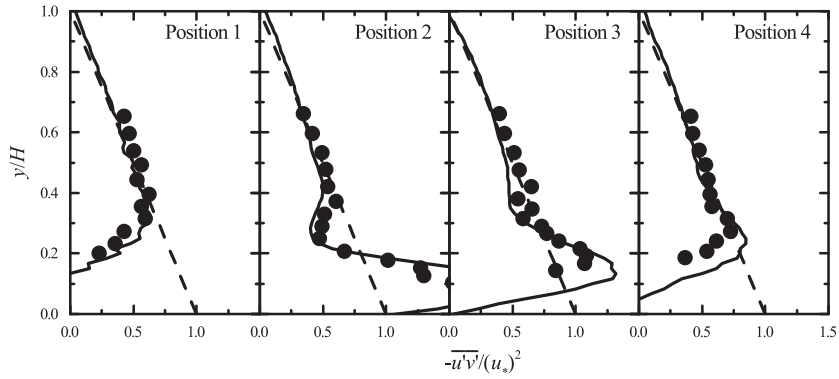


**Fig. 10.** Comparison between experimental data and LBM results in terms of the Reynolds shear stress profiles at Position 1–4: • Experiment; — LBM. The flat-bed profile (dashed line) is also shown for comparison.

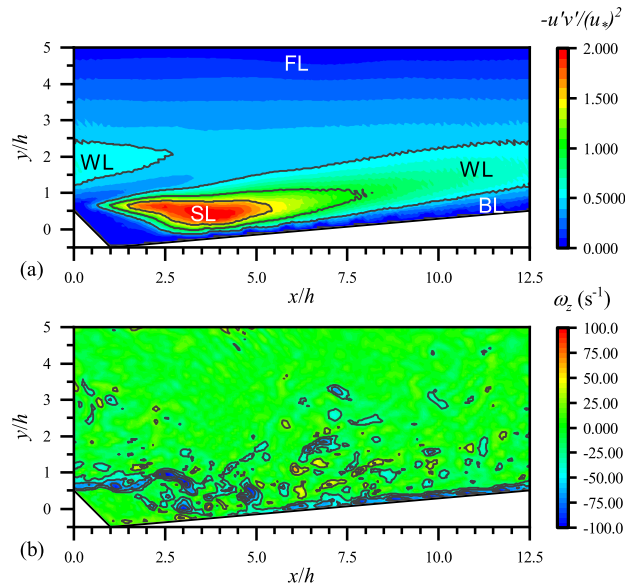


**Fig. 11.** Spatial distribution of (a) the normalized Reynolds shear stress and (b) the instantaneous vorticity in  $z$ -direction, in the longitudinal plane half-way through the spanwise length.

normalized Reynolds shear stress and the instantaneous vorticity in  $z$ -direction ( $\omega_z$ ), in the longitudinal plane half-way through the spanwise length, are plotted in Fig. 11(a) and (b), respectively.

Fig. 11(a) shows four distinct flow areas, including the free surface area (FS), the separated shear layer (SL), the developing boundary layer (BL), and the wake layer (WL). Similar features were observed in CFD/LES simulations performed by Stoesser et al. [12]. The FS is characterized by the layered small shear stress. The SL is produced by the strong flow separation at the dune crest, in which complex 3D flow instabilities take place, as shown in Fig. 11(b). The SL has the highest shear stress and it is the source of chaotic motions in the separation region just behind the dune. The vortices generated in the separation region are carried downstream by the mean flow, forming the WL with small eddies and moderate shear stresses. In the BL at the stoss side of the bed form beyond the reattachment, new vortices, whose sizes are much smaller than the ones in the separation region, are generated with an upward motion. Although the bed form geometry and the flow depth are slightly different, our LBM results are in very good qualitative agreement with previous CFD/LES simulations [12,13].

The kinetic energy (KE) spectrums at p1–p5 are shown in Fig. 12. The KE per unit volume is normalized by the variance of the instantaneous flow velocities. Clearly, it can be seen that there is a peak of KE at about 2 Hz at the middle depth of the flow (p2–p4). The KE peak occurs at a lower and a higher frequency as it is close to the bed (p1) and the free surface (p5), respectively. The decrease of frequency with the increase of flow depth could be due to the relatively larger eddy size and smaller mean flow velocity close to the bed form. A rough estimation based on a cut-off frequency (10 Hz) and the mean flow velocity (about 28 cm/s) indicates that the major portion of the KE is carried by eddies with size larger than 2.8 cm, which is much greater than the 1 mm lattice spacing used in our simulations. This indicates that the large eddies are well resolved in the LBM simulation.

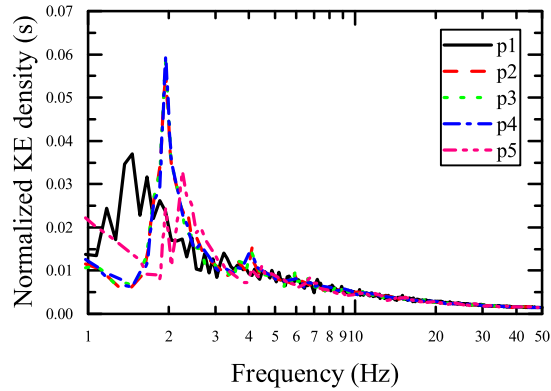


Fig. 12. Kinetic energy (KE) spectrums at p1–p5.

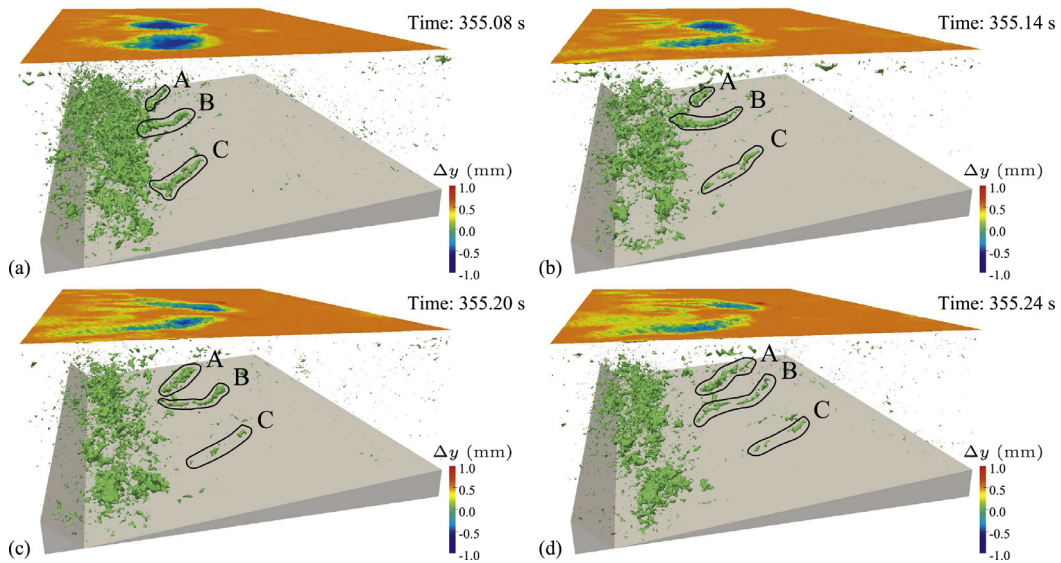


Fig. 13. Evolution of the instantaneous flow structures visualized by the isosurfaces of pressure fluctuation at  $p' = -10$  Pa. The free surfaces are plotted and colored by the corresponding elevations.

Following Stoesser et al. [12], Grigoriadis et al. [13], Omidyeganeh and Piomelli [14], the instantaneous flow structures are visualized by plotting the isosurfaces of pressure fluctuations at  $p' = -10$  Pa in Fig. 13. Owing to the flow instabilities at the SL, as shown in Fig. 11(b), a huge amount of roller vortices are induced near the dune crest. These vortices further develop via successive pairings and grow into a size comparable to the dune height (A, B and C at time: 355.08 s since the start of the LBM simulation), as also observed in LES simulations [12,13] using a Navier–Stokes approach. These flow structures tilt upwards at different angles to the bed form. At 0.06 s later in Fig. 13(b), structures A and B travel downstream and are elongated due to vortex stretching, while structure C has already been broken up into smaller vortices. Some of these small vortices persist in the flow for quite a long period before being fully dissipated due to viscous effects, as shown in Fig. 13(c) and (d). The whole process will repeat and last roughly for 0.2 s.

Some of the vortical structures originated from the separation region are able to travel to the upper half of the channel and interact with the free surface. Fig. 13 shows that the deformation of the free surface is essentially three dimensional, which varies a lot in both streamwise and spanwise directions. Generally speaking, there are downdraft and upwelling of the free surface at locations just behind and in front of the dune crest. As described by Yue et al. [11], these surface patterns are the footprints of the flow structures immediately underneath the free surface.

Although the theoretical analysis of the relationship between bed form roughness and TSL only relies on the flow velocity and Reynolds shear stress profiles in Section 5, in practice, it is these complex turbulent flow structures induced by the bed form that disperse sediments in the flow.

**Table 2**

Summary of the case study regarding to turbulent flow over bed forms with different geometries and steepnesses. The slope is the inclination of the simulated flume to drive the flow. The steepness is defined as  $h/L$ .

Case	Geometry	Slope	$h/L$	$u_*$ (cm/s)	$U$ (cm/s)	Fr	Re	$f_T$
1	Dune	0.00066	0.06	1.97	19.30	0.252	11,581	0.083
2	Dune	0.00079	0.08	2.16	19.44	0.253	11,661	0.098
3	Dune	0.00081	0.10	2.18	19.24	0.251	11,544	0.103
4	Circle	0.002	0.08	3.43	19.03	0.248	11,415	0.260
5	Triangle 1	0.00301	0.08	4.21	19.57	0.255	11,744	0.369
6	Triangle 2	0.0033	0.08	4.41	19.40	0.253	11,642	0.413

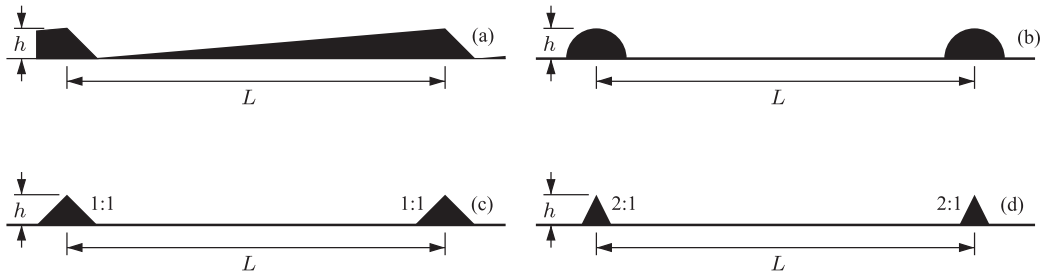


**Fig. 14.** Different shapes of bed form elements for the study of the effects of bed form roughness on sediment transport: (a) Dune-shape bed form element in Case 1–3; (b) Circular shape bed form element for Case 4; (c) Triangular shape 1 bed form element for Case 5; (d) Triangular shape 2 bed form element for Case 6.

**5. Effect of bed form roughness on total suspended load**

By comparing the LBM results with the experimental data and the CFD/LES results in Section 4, it can be shown that the LBM model is able to capture the essential turbulent characteristics of the flow over bed forms. In this section, a series of simulations is designed to investigate the effects of bed form roughness on the transport properties of turbulent flows over bed forms.

A total of six cases are studied with different bed form configurations, which are summarized in Table 2. For all cases, the bed form height ( $h$ ) and flow depth ( $H$ ) are fixed to be 1.2 cm and 6 cm, respectively. The channel width ( $W$ ) in spanwise direction is set to be four times of the flow depth so that the influence from the side walls on the turbulent structure is minimized. The bed form shape is adjusted to achieve different roughnesses by changing the elements of the bed form: in this study, dune (Case 1–3), circular (Case 4) and triangular (Case 5–6) elements are used (see Fig. 14). Based on experimental evidence on dune generation [41–43], the maximum steepness ( $h/L$ ) in nature is normally between 0.06 and 0.1. Hence, in Case 1–3, the steepness value is set to be 0.06, 0.08 and 0.1, respectively.

The mean flow velocity  $U$  and the flow depth  $H$  are adopted as the velocity and length scales to calculate the Reynolds number ( $Re = \rho HU/\mu$ ) and the Froude number ( $Fr = U/\sqrt{gH}$ ) based on the physical parameters of the flow. In order to compare different cases under similar hydrodynamic flow conditions, the simulated flume is tilted into different slopes such that similar values of  $Re$  and  $Fr$  are achieved. In this study, the average Reynolds number is 11,597 and all values lie within 1.5% of this value. The same conclusion applies to the Froude number.

**5.1. Total friction factor**

The total friction factor,  $f_T$ , also known as the Darcy friction factor [25,26], is usually used to describe the pressure loss in pipe flows. It is defined as:

$$f_T = \frac{8\tau_w}{\rho U^2} = 8\left(\frac{u_*}{U}\right)^2, \tag{34}$$

where  $\tau_w = \rho u_*^2$  is the wall shear stress. In the current work,  $f_T$  is used to characterize the flow resistance due to the presence of bed forms.

From Table 2, it is observed that the steepness increases the friction factor, so as the circular and triangular elements. The physical reason can be explained by plotting the streamlines of the flow, as shown in Fig. 15. The total flow resistance is composed of two components: one is the form drag due to pressure difference and the other is the skin friction. In the case of turbulent flow over bed forms, form drag dominates over the skin friction. For the triangular elements, a large recirculation region with low pressure is induced (see Figs. 15(e) and (f)), resulting in a huge form drag that slows down the flow significantly. In addition, a great amount of energy is lost in Case 4–6 due to the formation of more wakes behind the circular and triangular elements [44].

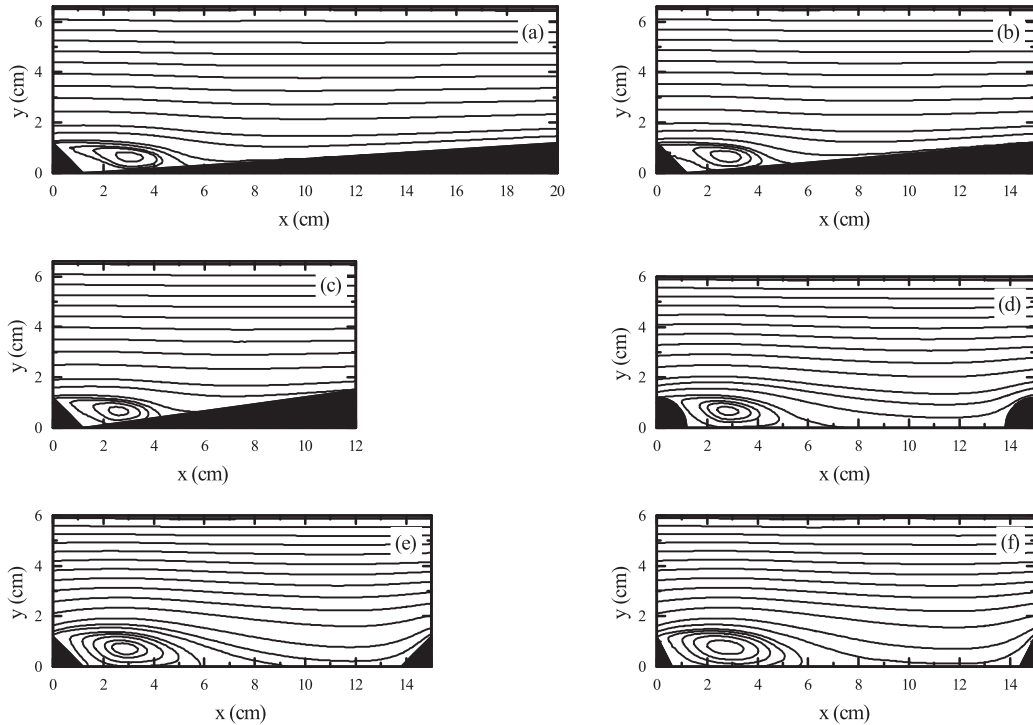


Fig. 15. Streamlines for the time-averaged flow field: (a) Case 1; (b) Case 2; (c) Case 3; (d) Case 4; (e) Case 5; (f) Case 6.

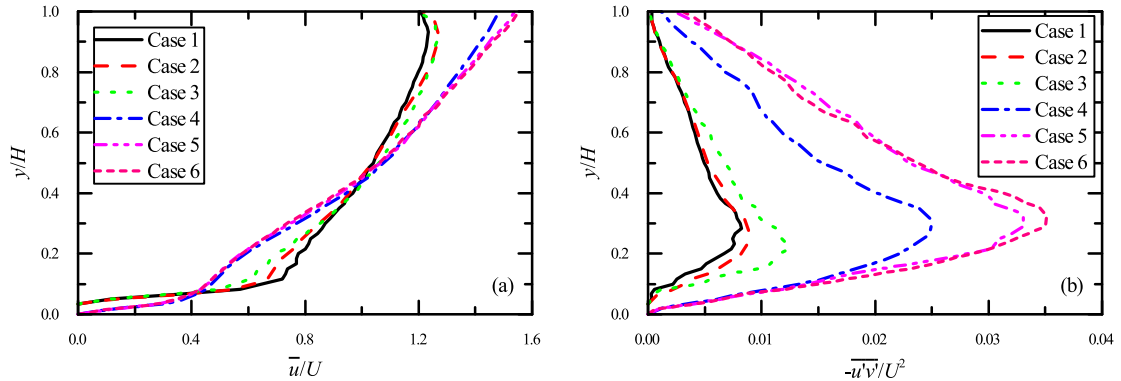


Fig. 16. Profiles of the normalized (a) time-averaged streamwise velocity and (b) Reynolds shear stress at Position 4, where  $x/L = 0.75$ .

5.2. Velocity and Reynolds shear stress profiles

The time-averaged flow velocity in streamwise direction ( $\bar{u}$ ) and the Reynolds shear stress ( $\tau_{Re}$ ) are normalized against the mean flow velocity ( $U$ ) and plotted in Fig. 16. It is shown in Fig. 16(a) that the normalized velocity profiles intersect at a point slightly below the middle depth ( $y/H = 0.5$ ) where  $\bar{u}/U$  is roughly 1. Generally speaking, the flow over dune-shape bed forms (Case 1–3) has a higher velocity at the inner flow region and lower velocity at the outer flow region compared to the flow over circular and triangular bed forms (Case 4–6), in which the friction factor is much higher. Hence, the velocity gradient in Case 1–3 is generally smaller than that in Case 4–6, despite the fact that they have almost the same mean flow velocity.

As for the Reynolds shear stress (see Fig. 16(b)), it increases from zero at the bottom to a maximum value at a level around  $y/H = 0.2$  and decreases to a non-zero value at the free surface. It is observed that the Reynolds shear stress consistently increases with the friction factor  $f_T$ .

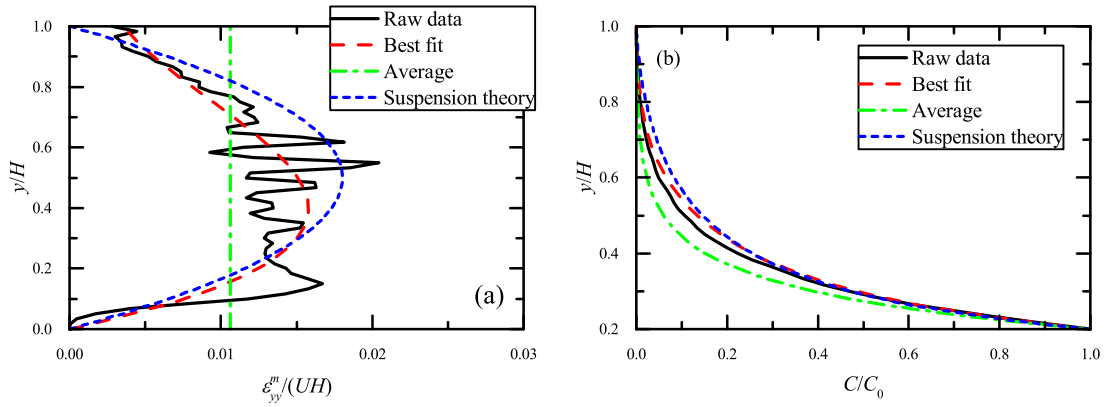


Fig. 17. Profiles of (a) the eddy diffusivity and (b) the sediment concentration for Case 4, when  $Z = 0.1$ .

### 5.3. Diffusion coefficient and sediment concentration

In this study, instead of relying on the conventional flat-bed assumption for the velocity and Reynolds shear stress profiles [4,24], the raw simulation data in Fig. 16 is used to calculate the eddy diffusivity based on Eq. (12). Fig. 17(a) shows the calculated distribution of normalized eddy diffusivity (black solid line) for Case 4, which fluctuates a lot. A best fit line using a third order polynomial (red dashed line) and the spatially-averaged value (green dash-dotted line) can also be used to calculate the distribution of sediment concentrations. In addition, a theoretical diffusivity profile (blue short-dashed line) is also plotted in Fig. 17(a), based on the linear distribution of Reynolds shear stress (with zero value at the free surface and  $\rho u_*^2$  at the mean bed level) and the well-known Prandtl-von Karman velocity defect law (with the von Kármán constant equal to 0.4) [24].

Integrating Eq. (9) by separation of variables, the sediment concentration can be written as:

$$\int_{C_0}^C \frac{1}{C} dC = -\frac{w}{\gamma} \int_{y_0}^y \frac{1}{\varepsilon_{yy}^m} dy. \tag{35}$$

A boundary condition is required to solve Eq. (35). In this study, a reference level  $y_0/L$  equal to 0.2 (top of the bed form) is selected where the sediment concentration is  $C_0$ . The integral of the reciprocal of the eddy diffusivity cannot be calculated explicitly, therefore it is estimated by the trapezoidal rule as:

$$\ln\left(\frac{C_n}{C_0}\right) = -\frac{\Delta y}{2H} \frac{w}{\gamma U} \left( \frac{UH}{\varepsilon_{yy,1}^m} + 2 \sum_{i=2}^{n-1} \frac{UH}{\varepsilon_{yy,i}^m} + \frac{UH}{\varepsilon_{yy,n}^m} \right), \tag{36}$$

where  $\Delta y$  is taken as the size of the lattice grid and equal to 1 mm for all cases. The sediment concentration and the eddy diffusivity at level  $y_n$  are denoted as  $C_n$  and  $\varepsilon_{yy,n}^m$ , respectively, and  $y_n = y_{n-1} + \Delta y$ . The ratio between the downward settling velocity ( $w/U$ ) and upward turbulence induced diffusion ( $\gamma$ ) is denoted by a weighting factor  $Z$ , given as below:

$$Z = \frac{w}{\gamma U}. \tag{37}$$

Substituting Eq. (37) into Eq. (36), the distribution of sediment concentration, for a given  $Z$  value, can be calculated by:

$$C_n = C_0 \exp \left[ -Z \frac{\Delta y}{2H} \left( \frac{UH}{\varepsilon_{yy,1}^m} + 2 \sum_{i=2}^{n-1} \frac{UH}{\varepsilon_{yy,i}^m} + \frac{UH}{\varepsilon_{yy,n}^m} \right) \right], \tag{38}$$

As shown in Fig. 17(b), using a uniform distribution of eddy diffusivity may underestimate the sediment concentration in this case. At the middle depth ( $y/H = 0.5$ ), the sediment concentration based on the averaged eddy diffusivity is only about half of that calculated from the raw data. Meanwhile, the best fit curve does capture the overall trend of the diffusivity and results into a sediment concentration profile close to that based on the raw data, with a slight overestimation. In addition, the sediment concentration resulting from the commonly used theoretical velocity and Reynolds shear stress profiles in suspension theory (called as the flat-bed model [24]) is generally higher than that calculated from the raw data due to the highly overestimated eddy diffusivity.

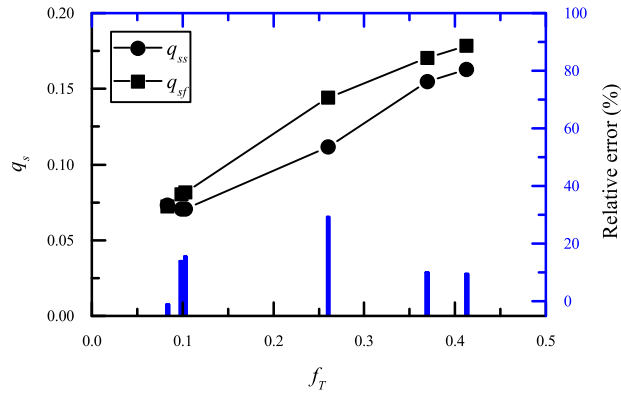


**Fig. 18.** The total suspended load calculated directly from the numerical results and with the flat-bed assumptions at different friction factors with  $Z = 0.1$ . The relative errors are shown in (blue) bars referring to the right hand side axis. (For interpretation of the references to color in this figure legend, the reader is referred to the web version of this article.)

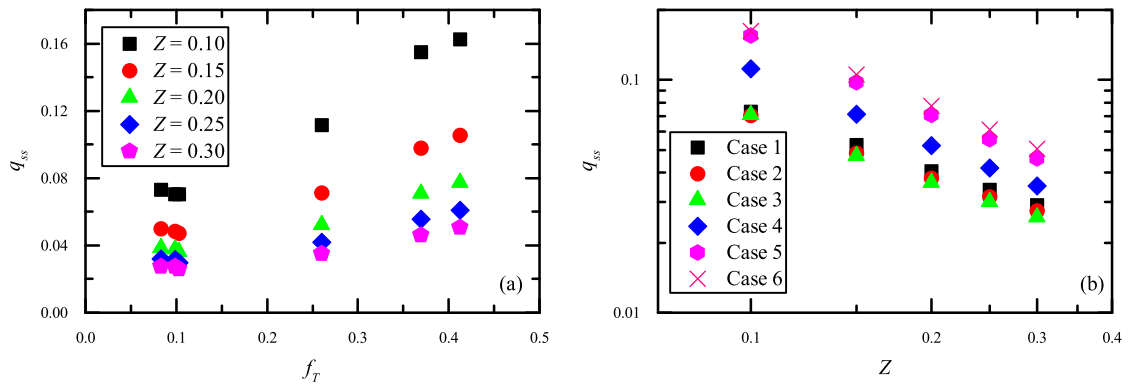


**Fig. 19.** Variation of the normalized TSL against (a) the friction factor  $f_T$  and (b) the value of  $Z = w/(\gamma U)$ .

5.4. Total suspended load

The normalized TSL ( $q_s$ ) can be calculated by integrating the product  $C(y)\bar{u}(y)$  over the depth above the reference level  $y_0$  divided by the corresponding dimensional parameters:

$$q_s = \frac{1}{UC_0H} \int_{y_0}^{y_s} \bar{u}Cdy = \sum_{i=1}^N \frac{\bar{u}_i C_i}{U C_0 H} \Delta y, \tag{39}$$

where  $N$  represents the number of lattice nodes from the reference level to the free-surface ( $y_s$ ). Here, the mean flow velocity  $U$ , the SSC at the reference level  $C_0$ , and the flow depth  $H$  are chosen for normalization. Since the flow is in steady state, the calculated  $q_s$  at Position 4 should be similar for all the other positions.

The normalized total suspended loads with the flat-bed assumptions ( $q_{sf}$ ) for Case 1–6 are compared to that calculated from the raw simulation data ( $q_{ss}$ ) in Fig. 18 at different friction factors and with  $Z$  equal to 0.1. The relative errors, calculated by  $(q_{sf}/q_{ss}) - 1$ , are also plotted in Fig. 18. It can be seen that, for the calculation of TSL in turbulent flow over bed forms, the adoption of simplified flat-bed assumptions will lead to an overestimation, which qualitatively agrees with the experimental observations from Lyn [4], despite the smaller relative errors in this work. The maximum relative error is about 30% when  $f_T = 0.26$  in Case 4.

The normalized TSL directly calculated from the numerical results,  $q_{ss}$ , is plotted against the total friction factor  $f_T$  in Fig. 19(a), for different values of  $Z$ . It can be found that, as the friction factor increases, the TSL also increases. This is due to the fact that the highly frictional bed forms are able to disturb the flow more and create larger Reynolds shear stress (see Fig. 16(b)) and, hence, a larger eddy diffusivity which helps to enhance the capacity of the flow to carry sediments. Therefore, the friction factor is an indirect measure of the mixing induced by the bed forms.

Besides, the TSL is inversely proportional to  $Z$ , which is shown Fig. 19(b). As  $Z$  becomes large, for example, when the sediments are heavy, the downward settling of sediments will dominate over the upward diffusion, resulting into a reduction in  $q_{ss}$ . On the other hand, when  $Z$  is small, the diffusion mechanism becomes the dominating factor and more sediments will diffuse into the fluid body, resulting in a large  $q_{ss}$ .

**Table 3**  
Fitting results for  $a_1$ ,  $a_2$  and  $a_3$ .

Fitting parameter	Value	Standard error
$a_1$	0.0045	3.12E-4
$a_2$	0.024	0.0014
$a_3$	1.034	0.0275

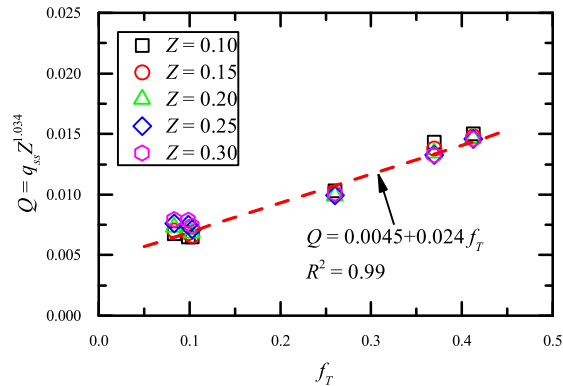


**Fig. 20.** Plot of  $Q$  against the friction factor  $f_T$ .

The results in Fig. 19 indicate that there is a self-similar behavior of  $q_{ss}$  with respect to  $f_T$ , depending on  $Z$ . This suggests that there must be a scaling  $q_{ss}Z^{a_3}$  that will collapse all the data set. By choosing a general law given by:

$$Q = q_{ss}Z^{a_3} = a_1 + a_2 f_T, \quad (40)$$

where the fitting parameters  $a_1$ ,  $a_2$  and  $a_3$  can be calculated by least squares. The results are presented in Table 3 and Fig. 20 shows the collapsed data into a straight line with  $R^2$  as high as 0.99. It indicates that there is a linear dependence of the TSL  $q_{ss}$  on the total friction factor  $f_T$ , which is independent on the choice of the weighting factor  $Z$ .

Although Eq. (40) reveals a simple relationship between the bed form roughness and the TSL, it only considers the influence of advection and diffusion of suspended sediments in the fluid body, reflecting the altered flow pattern due to the presence of bed forms. It should be noted that for the calculation of  $q_{ss}$  in Eq. (40), the SSC is normalized by  $C_0$  (see Eq. (39)), which itself also depends on the bed form roughness [45–47]. Therefore, the effect of the bed form roughness on the absolute value of the TSL is rather a complex problem and deserves further investigation.

## 6. Conclusions

The present study is one of the very first attempts to study turbulent flow over bed forms using the three-dimensional lattice Boltzmann method. A Smagorinsky SGS model is incorporated into LBM to simulate high Reynolds number flows. Besides, instead of using a simplified rigid free-slip boundary condition for the fluid-gas interface, a free-surface model is applied. These models are verified by simulations of a two-dimensional driven cavity flow problem and a three-dimensional dam break problem, in which the LBM results agree with the available CFD and experimental data.

LBM is also successfully applied to simulate the turbulent flow over bed forms to investigate their influence on the total suspended load, which may provide valuable insights to engineers, geologists and ecologists. The enhanced mixing generated by the presence of bed forms induces larger diffusivities on the normal direction of the flow that will increase the overall suspended load. We succeeded in quantifying this effect via the friction factor  $f_T$ . It is found that the adoption of the theoretical flat-bed assumptions generally overestimates the total suspended load of turbulent flow over bed forms and the degree of overestimation depends on the friction factor. The relative error between the predictions based on the flat-bed assumptions and the raw data from LBM simulations can be as high as 30%, based on a particular case in this study. Besides, the total suspended load  $q_s$  is found to be linearly proportional to the friction factor  $f_T$  and nearly inversely proportional to the weighting factor  $Z$ .

In summary, the findings of this study have the potential to facilitate a more efficient and accurate estimation of the total suspended load in natural rivers and man-made channels. Nevertheless, it still remains to be fully understood the effect of the hydrodynamic parameters  $Re$  and  $Fr$ , which will alter the flow pattern significantly. In future works, numerical simulations at other Reynolds numbers and Froude numbers will be carried out to further generalize the relationship between  $q_s$ ,  $f_T$  and  $Z$ .

## Acknowledgments

This research is conducted in part using the research computing facilities and/or advisory services offered by Information Technology Services, the University of Hong Kong and under the support of FAP-DF, Brazil. We would like to thank Prof. T.F. Oliveira, Prof. R.F. Bobenrieth-Miserda and Prof. C.H.R. Lima for the insightful discussions.

## References

- [1] S.R. McLean, J.M. Nelson, S.R. Wolfe, Turbulence structure over twodimensional bed forms: Implications for sediment transport, *J. Geophys. Res. Oceans* 99 (C6) (1994) 12729–12747.
- [2] M.M. Ellis, Erosion silt as a factor in aquatic environments, *Ecology* 17 (1) (1936) 29–42.
- [3] J.M. Nelson, S.R. McLean, S.R. Wolfe, Mean flow and turbulence fields over twodimensional bed forms, *Water Resour. Res.* 29 (12) (1993) 3935–3953.
- [4] D.A. Lyn, Turbulence measurements in open-channel flows over artificial bed forms, *J. Hydraul. Eng.* 119 (3) (1993) 306–326.
- [5] J.D. Smith, S.R. McLean, Spatially averaged flow over a wavy surface, *J. Geophys. Res.* 82 (12) (1977) 1735–1746.
- [6] R.R. Holmes, M.H. Garcia, Flow over bedforms in a large sand-bed river: a field investigation, *J. Hydraul. Res.* 46 (3) (2008) 322–333.
- [7] R. Kostaschuk, P. Villard, Flow and sediment transport over large subaqueous dunes: Fraser River, Canada, *Sedimentology* 43 (5) (1996) 849–863.
- [8] J. Best, The fluid dynamics of river dunes: a review and some future research directions, *J. Geophys. Res. Earth Surf.* 110 (F4) (2005).
- [9] J.Y. Yoon, V.C. Patel, Numerical model of turbulent flow over sand dune, *J. Hydraul. Eng.* 122 (1) (1996) 10–18.
- [10] C. Mendoza, H.W. Shen, Investigation of turbulent flow over dunes, *J. Hydraul. Eng.* 116 (4) (1990) 459–477.
- [11] W. Yue, C.L. Lin, V.C. Patel, Large eddy simulation of turbulent open-channel flow with free surface simulated by level set method, *Phys. Fluids* 17 (2) (2005) 025108.
- [12] T. Stoesser, C. Braun, M. García-Villalba, W. Rodi, Turbulence structures in flow over two-dimensional dunes, *J. Hydraul. Eng.* 134 (1) (2008) 42–55.
- [13] D.G.E. Grigoriadis, E. Balaras, A.A. Dimas, Largeeddy simulations of unidirectional water flow over dunes, *J. Geophys. Res. Earth Surf.* 114 (F2) (2009).
- [14] M. Omidyeganeh, U. Piomelli, Large-eddy simulation of two-dimensional dunes in a steady, unidirectional flow, *J. Turbul.* 12 (2011).
- [15] D.C. Wilcox, *Turbulence Modeling for CFD*, (third ed.), D C W Industries, 2006.
- [16] C.D. Argyropoulos, N.C. Markatos, Recent advances on the numerical modelling of turbulent flows, *Appl. Math. Modell.* 39 (2) (2015) 693–732.
- [17] B. Chaouat, The state of the art of hybrid RANS/LES modeling for the simulation of turbulent flows, *flow, Turbul. Combust.* 99 (2) (2017) 279–327.
- [18] W. Rodi, *The Prediction of Free Turbulent Boundary Layers by Use of a Two-Equation Model of Turbulence*, University of London, 1972 Phd. thesis.
- [19] P. Sagaut, *Large Eddy Simulation for Incompressible Flows: An Introduction*, Springer Science & Business Media, 2006.
- [20] M. Lesieur, O. Metais, New trends in large-eddy simulations of turbulence, *Ann. Rev. Fluid Mech.* 28 (1) (1996) 45–82.
- [21] W. Yue, C. Lin, V.C. Patel, Numerical simulation of unsteady multidimensional free surface motions by level set method, *Int. J. Numer. Methods Fluids* 42 (8) (2003) 853–884.
- [22] S. Chen, G.D. Doolen, Lattice Boltzmann method for fluid flows, *Ann. Rev. Fluid Mech.* 30 (1) (1998) 329–364.
- [23] S. Geller, M. Krafczyk, J. Tlke, S. Turek, J. Hron, Benchmark computations based on lattice-Boltzmann, finite element and finite volume methods for laminar flows, *Comput. Fluids* 35 (8) (2006) 888–897.
- [24] V.A. Vanoni, *Sedimentation Engineering*, 2006, American Society of Civil Engineers.
- [25] M. Ahsan, Numerical analysis of friction factor for a fully developed turbulent flow using  $k\epsilon$  turbulence model with enhanced wall treatment, *Beni Suef Univ. J. Basic Appl. Sci.* 3 (4) (2014) 269–277.
- [26] C.A. Yunus, J.G. Afshin, *Heat and Mass Transfer: Fundamentals and Applications*, McGraw-Hill, 2011, pp. 488–489.
- [27] S. Hou, J. Sterling, S. Chen, G.D. Doolen, A lattice Boltzmann sub-grid model for high Reynolds number flows, *Pattern Formation Lattice Gas Autom.* 6 (1996) 149.
- [28] C. Körner, M. Thies, T. Hofmann, N. Thürey, U. Rüdte, Lattice Boltzmann model for free surface flow for modeling foaming, *J. Stat. Phys.* 121 (1) (2005) 179–196.
- [29] H. Tennekes, J. Lumley, *A First Course in Turbulence*, Pe Men Book Company, 1972.
- [30] W. Schmidt, *Der Massenaustausch in freier Luft und verwandte Erscheinungen*, Grand, 1925.
- [31] U. Frisch, A. Kolmogorov, *Turbulence: The Legacy of A. N. Kolmogorov*, Cambridge University Press, 1995.
- [32] P.L. Bhatnagar, E.P. Gross, M. Krook, A model for collision processes in gases. i. small amplitude processes in charged and neutral one-component systems, *Phys. Rev.* 94 (3) (1954) 511–525.
- [33] N. Thürey, T. Pohl, U. Rüdte, M. Öchsner, C. Körner, Optimization and stabilization of LBM free surface flow simulations using adaptive parameterization, *Comput. Fluids* 35 (8) (2006) 934–939.
- [34] E. Erturk, Discussions on driven cavity flow, *Int. J. Numer. Methods Fluids* 60 (3) (2009) 275–294.
- [35] F. Auteri, N. Parolini, L. Quartapelle, Numerical investigation on the stability of singular driven cavity flow, *J. Comput. Phys.* 183 (1) (2002) 1–25.
- [36] Y.F. Peng, Y.H. Shiau, R.R. Hwang, Transition in a 2-d lid-driven cavity flow, *Comput. Fluids* 32 (3) (2003) 337–352.
- [37] D.A. Perumal, A.K. Dass, Application of lattice Boltzmann method for incompressible viscous flows, *Appl. Math. Modell.* 37 (6) (2013) 4075–4092.
- [38] E. Erturk, T.C. Corke, C. Gökçöl, Numerical solutions of 2d steady incompressible driven cavity flow at high Reynolds numbers, *Int. J. Numer. Methods Fluids* 48 (7) (2005) 747–774.
- [39] Y. Nishi, P.V. Doan, Hybrid boundary condition combined with data assimilation for simulations of free surface flows using lattice Boltzmann method, *Comput. Fluids* 88 (2013) 108–114.
- [40] J. Martin, W. Moyce, Part iv. an experimental study of the collapse of liquid columns on a rigid horizontal plane, *philosophical transactions of the royal society of London a: mathematical, Phys. Eng. Sci.* 244 (882) (1952) 312–324.
- [41] J. Fredsoe, Shape and dimensions of stationary dunes in rivers, *J. Hydraul. Div.* 108 (8) (1982) 932–947.
- [42] M.S. Yalin, *Mechanics of Sediment Transport*, Pergamon Press, 1972.
- [43] V.A. Vanoni, L.S. Hwang, Bed forms and friction in streams, *J. Hydraul. Div. Am. Soc. Civil Eng.* 93 (1967) 121–144.
- [44] H.M. Morris, *A New Concept of Flow in Rough Conduits*, University of Minnesota., 1950.
- [45] P.E. Grams, P.R. Wilcock, Transport of fine sediment over a coarse, immobile riverbed, *J. Geophys. Res. Earth Surf.* 119 (2) (2014) 188–211.
- [46] P.E. Grams, P.R. Wilcock, Equilibrium entrainment of fine sediment over a coarse immobile bed, *Water Resour. Res.* 43 (10) (2017).
- [47] M. Garcia, G. Parker, Entrainment of bed sediment into suspension, *J. Hydraul. Eng.* 117 (4) (1991) 414–435.